Thermomechanical finite element modelling of wheel-rail contact and experimental validation

He, Chunyan; Yang, Zhen; Zhang, Pan; Dollevoet, Rolf; Li, Zili

DOI
10.1016/j.triboint.2025.110666

Publication date
2025

Document Version
Final published version

Published in
Tribology International

Citation (APA)
He, C., Yang, Z., Zhang, P., Dollevoet, R., & Li, Z. (2025). Thermomechanical finite element modelling of wheel-rail contact and experimental validation. *Tribology International*, *209*, Article 110666. https://doi.org/10.1016/j.triboint.2025.110666

Tribology International 209 (2025) 110666

Contents lists available at ScienceDirect

Tribology International

journal homepage: www.elsevier.com/locate/triboint

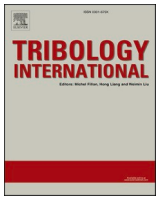

Thermomechanical finite element modelling of wheel-rail contact and experimental validation

Chunyan He, Zhen Yang *, Pan Zhang, Rolf Dollevoet, Zili Li

Delft University of Technology, Section of Railway Engineering, Stevinweg 1, Delft 2628 CN, the Netherlands

ARTICLE INFO

Keywords:
Finite element model
Contact temperature
Friction
Wheel-rail contact

ABSTRACT

Frictional heat is generated at the wheel-rail interface during train operations, particularly under high slip ratios during acceleration and braking. Thermal effects can accelerate wear, induce plastic deformation, and contribute to thermal fatigue. Reliable modelling of wheel-rail contact that considers friction-induced thermal effects is desirable for the accurate prediction of wheel-rail interface deterioration. Several analytical and numerical models have been proposed to simulate thermal or thermomechanical wheel-rail loads but have rarely been validated, especially in high slip ratio scenarios where flash temperatures exceed 200 °C. This study develops and experimentally validates a three-dimensional thermomechanical finite element (FE) wheel-rail contact model for high slip ratio conditions, with contact temperatures reaching 360 °C. The model incorporates key mechanical parameters, including wheel loads, coefficients of friction, and slip ratios. Simulated rail surface temperatures across various slip ratios (5 %, 10 %, and 15 %) are compared with the flash temperatures measured with an onboard infrared thermal camera, showing good agreement with a maximum deviation of 9.9 %. This confirms the reliability of the model for simulating wheel-rail contact under thermal effects.

1. Introduction

Frictional heat generation at the wheel-rail interface is a significant occurrence during train operations, especially during acceleration and braking. Substantial wheel-rail thermal loading occurs at high slip ratios because of the rapid accumulation of thermal energy and the consequent increase in temperature in the contact area. This thermal loading is known to accelerate wear and plastic deformation and cause thermal fatigue in wheel/rail materials [1,2]. Wheel/rail materials can be easily worn when the wheel-rail contact temperature exceeds 350 °C [3]. Thermal fatigue occurs when thermal loading alters the shakedown behaviour and mechanical properties of materials [4,5]. The elastic and shakedown limits of a wheel and rail can be reduced under thermal loading, increasing the vulnerability of the steel to progressive plastic deformation. This may lead to crack initiation and potential structural failure, even under relatively low mechanical stresses. In addition, high temperatures may induce microstructural transformations in wheel/rail materials, such as the transformation of pearlite and ferrite into austenite, followed by partial conversion into martensite beneath wheel and rail surfaces (occurring above 720 °C with rapid cooling) [6,7]. This deterioration of the wheel-rail interface increases maintenance costs and impacts the operational safety of trains. Therefore, it is important to investigate wheel-rail friction-induced temperature and its effects on wheel/rail damage.

Accurately measuring the contact temperature between the wheel and rail under operational conditions is a complex, labour-intensive, and expensive process [8], which has led to the development of analytical and numerical modelling methods to examine the thermal loading and temperature field at the wheel-rail interface. Several analytical approaches have been formulated to calculate the maximum flash temperature induced by a moving heat flux in a single body. Jaeger [9] investigated the problem of idealized plane heat sources of various shapes, such as two-dimensional (2D) uniformly distributed band sources and three-dimensional (3D) rectangular sources, moving at constant or nonconstant velocities on the surface of a semi-infinite medium. Subsequent analyses then extended Jaeger's approach in two aspects: 1) by applying different moving heat sources [10,11] and 2) by including the thermal radiation and convection to the ambient environment [12,13]. A 2D elliptical band source was modelled in [10] to represent the heat induced by contact. Instead of applying a predefined heat source as in [9,10], Knothe et al. [11] calculated the 2D heat source at the wheel-rail interface on the basis of Hertzian contact pressure and

* Corresponding author.
E-mail address: Z.Yang-1@tudelft.nl (Z. Yang).

https://doi.org/10.1016/j.triboint.2025.110666
Received 4 February 2025; Received in revised form 12 March 2025; Accepted 19 March 2025
Available online 22 March 2025

analytically derived the temperature field engendered by wheel-rail sliding interactions through the application of Laplace transforms and Green's function. Their study revealed that the wheel-rail contact temperatures do not exceed 450–500 °C if the slip ratio is less than 2 % and the coefficient of friction is less than 0.6. By considering the heat interaction with the ambient environment (i.e., radiation and convection), Lewisa et al. [12] calculated the temperature field induced by twin-disc rolling contact from partial to full slip (slip ratio from 0.5 % to 5 %) and determined that the maximum contact temperature above ambient temperature reached 113 °C under a normal contact stress of 1500 MPa and a disc surface velocity of 0.98 m/s. To investigate the effects of contact body geometry on contact temperature, thinner and smaller twin discs operating under the same conditions as [12] were simulated in [13], which reported higher simulated contact temperatures (199.2 °C for the thinner discs and 235.3 °C for the smaller discs) than the results obtained in [12]. These analytical studies [9–13] indicated that the instantaneous temperatures generated at the contact interface are related to the coefficient of friction, contact pressure, thermal properties, sliding velocity, and contact body geometry.

In contrast to analytical models, finite element (FE) models can address transient thermal contact issues while considering complex geometries and material complexity, including plasticity, temperature dependence [14], and dynamic wheel-rail interactions. Vo et al. [15] developed a 3D FE model for a rail subjected to multiple thermal loads from passing locomotives, employing Goldak's heat source model [16]. A simulation with a slip ratio of 8.5 % indicated that the rail-surface temperature can reach 522 °C after one wheel pass and 723 °C after six passes. However, the heat source of the model was calculated on the basis of Hertzian contact pressure. Such a simplification can potentially lead to deviations in the thermal results from the actual values. Naeimi et al. [14] proposed a 3D dynamic thermomechanical FE wheel-rail contact model in which the heat source was calculated on the basis of the tangential load and micro-slip between the elements in contact. The simulated peak contact temperatures with slip ratios of 10 %, 18 %, and 26 % were 284 °C, 498 °C, and 756 °C, respectively. Lian et al. [8] presented a 3D FE wheel-rail contact model to consider the superimposed thermomechanical loads induced by multiple wheel passages. Their study indicated that the maximum temperature of the rail surface after 9 wheel passages can reach 776 °C, with a slip ratio of 9.43 %.

In terms of model validation, attempts were made in [17] to validate the analytical model presented in [12] for low slip ratio (below 5 %) wheel-rail contact scenarios via infrared cameras. The results indicated that the measured contact temperature ranged between 100 and 150 °C with a slip ratio of 5 %, which aligned well with the simulated results in [12]. However, although FE models of thermal contact between wheels and braking blocks [18–20] or braking pads [21] have been experimentally validated via infrared cameras, no validation, to the best of the author's knowledge, has been reported for FE wheel-rail thermal contact models with high slip ratios (above 5 %) that may induce significant thermal damage.

In this study, a 3D thermomechanical FE wheel-rail contact model was constructed, and the model was validated with a carefully designed laboratory test. Wheel-rail contact across a range of slip ratios from 2 % to 35 % during braking was reproduced using the TU-Delft V-Track test rig, which is a downscaled wheel-rail interaction test rig, and the corresponding contact temperature was captured with an onboard high-precision infrared thermal camera. This measurement captured real-time flash temperatures induced by wheel-rail contact up to 670 °C. Section 2 presents the thermomechanical FE contact model, the methodology for measuring wheel-rail contact temperature, and the approach for calculating the slip ratio. Section 3 first presents the measurement data processing and then examines the correlation between the measured temperatures and slip ratios. A comparative analysis between the simulated and measured wheel-rail contact temperatures is subsequently presented. Section 4 presents the main conclusions. The primary aim of this study is to experimentally validate the proposed FE model by comparing the simulated wheel-rail contact temperatures with those obtained from experiments conducted on a V-Track test rig.

2. Method

2.1. Numerical model

A 3D thermomechanical FE wheel-rail contact model was constructed, incorporating its geometrical, mechanical, and material characteristics (R260 and R350HT rail grades) in the V-Track, as depicted in Fig. 1. This model is capable of replicating the motion of a wheel travelling along a track at a predefined slip ratio during braking. The same braking process of the wheel was measured on the V-Track, as described in Section 2.2. The simulation procedure of the FE model includes four steps: 1. Modelling of wheel-rail contact in the V-Track test rig (preprocessing in ANSYS); 2. Static equilibrium of the wheel loading on the rail (implicit solution); 3. Dynamic rolling of the wheel along the rail (explicit solution); 4. Results output and analysis (postprocessing with MATLAB). The implicit-explicit sequential analysis (combining steps 2 and 3) can effectively mitigate initial dynamic excitation.

The preprocessing of FE modelling included geometry and material modelling, structural discretization, and the definitions of boundary conditions (including contact pairs), loads, and initial conditions. In terms of the geometry within the FE model, the track model spanned a total length of 1.75 m, encompassing 14 sleeper spans, and included a 0.065 m solution zone along the rail. The rail was fixed to the sleepers through fastenings in three directions. The sleepers were supported by the ballast and the subgrade, which were represented by the rubber pads and plywood layers in the test rig. A wheel with a radius of 65 mm (1/7 scale of the field wheels) and a half axle were modelled. Two distinct sets of temperature-dependent material parameters that have been widely used for wheel-rail thermomechanical behaviour modelling [8,14,15, 22–25] were employed, with one set detailed in Tables 1 and 2 [8,14,15, 23,25] and the other set listed in Table 3 [22,24]. The thermal conductivities in Tables 2 and 3 were downscaled (1/7 scale) in this study on the basis of the similarity law [26]. The parameters in Eq. (2) of this study can be appropriately scaled, while temperature remains unscaled, according to [26]. Consequently, the measured temperature in the V-Track test rig can directly represent the corresponding values in the full-scale wheel-rail contact under field conditions. The simulation results obtained with different sets of material parameters are compared in Section 3. In the discretization process of the model, the primary suspension springs in the V-Track test rig were modelled via compressed spring-damper elements. These elements connected the wheel axle to lumped mass elements, which were simplified from the wheel axle box and the guiding block of the V-Track test rig, as described in Section 2.2. The wheel, rail, and sleepers were modelled with 8-node solid elements. The fastenings, ballast, and subgrade were modelled with spring-damper elements. To improve the calculation efficiency, a partially refined mesh strategy was applied. The finest mesh size of the top surface in the solution zone of the rail was 0.18 mm (x-axis) × 0.20 mm (y-axis) × 0.20 mm (z-axis). The FE model comprises 577,907 elements and 646, 016 nodes. The minor axis of the contact patch covers 13 contact elements; thus, sufficiently accurate contact solutions can be obtained for engineering applications [27].

An implicit–explicit sequential analysis was conducted to simulate wheel braking along the rail. The longitudinal (rolling direction) and lateral degrees of freedom of the wheel were first constrained to calculate the static equilibrium in the implicit analysis, where a gravity wheel load of 4000 N was applied. The longitudinal constraints of the wheel were then released in the explicit model for wheel rolling simulations, where a friction coefficient of 0.45 between the wheel and rail was applied. This applied friction coefficient was measured from the V-Track, based on the wheel-rail friction force and normal contact force recorded using dynamometers. When friction saturation occurred under

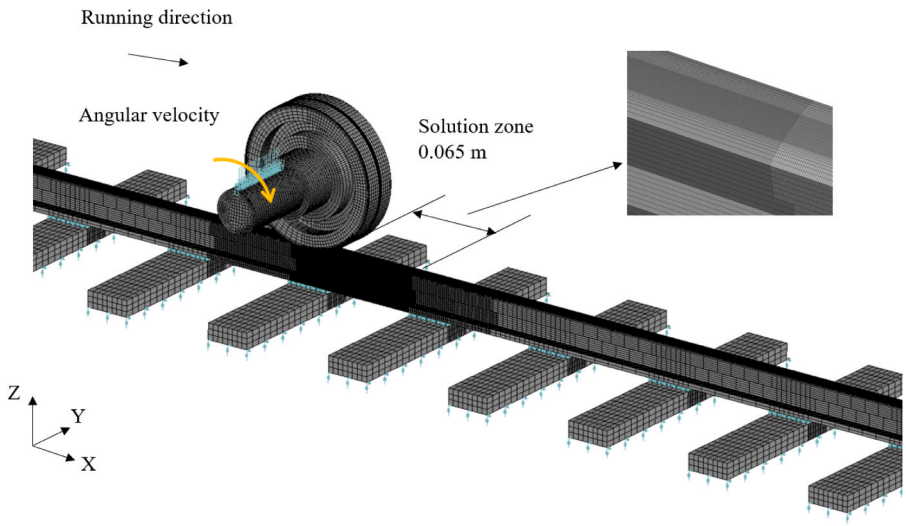

Fig. 1. Thermomechanical FE model of wheel-rail contact on the test rig.

Table 1
Temperature-dependent mechanical material parameters.

Temperature, T (°C)	Young's modulus, E (GPa)	Poisson's ratio, ν	Coefficient of thermal expansion, α ($\times 10^{-6}$ °C^{-1})	Hardening modulus, Ep (GPa)	Yield strength of R260	Yield strength of R350HT	Yield strength of wheel
24	213	0.295	9.89	22.7	583.0	779.0	500.0
230	201	0.307	10.82	26.9	585.1	781.1	502.1
358	193	0.314	11.15	21.3	518.8	714.8	435.8
452	172	0.320	11.27	15.6	432.4	628.4	349.4
567	102	0.326	11.31	6.2	251.1	447.1	168.1
704	50	0.334	11.28	1.0	136.2	332.2	53.2
900	43	0.345	11.25	0.1	113.4	309.4	30.4

Table 2
Temperature-dependent thermal material parameters.

Temperature, T (°C)	Specific heat capacity, c (J/kg°C)	Thermal conductivity, λ (W/m°C)
0	419.5	8.53
350	629.5	5.84
703	744.5	4.32
704	652.9	4.31
710	653.2	4.29
800	657.7	3.57
950	665.2	3.86
1200	677.3	4.35

high slip ratio conditions, the adhesion coefficient, i.e., the ratio of friction force to normal load, can be taken as the measured friction coefficient. The measured lateral friction force was close to zero with a careful control of the angle of attack in the V-Track. A fixed boundary condition was thus applied to the wheel axle in the lateral direction to minimize the simulated wheel-rail lateral force and its influence on the contact temperatures. The nodal displacements, obtained from the static equilibrium calculation, served as an initial condition for the explicit model. Another initial condition was the initial temperature of the wheel and rail, which was assumed to be 200 °C. The measurement was conducted with a continuous increase in slip ratio from 2 % to 35 %, and the simulation conditions were designed to be consistent with the experimental setup. In the test, by the time the slip ratio reached 5 %, the wheel had already been braking for a period, leading to heat accumulation in both the wheel and rail. Therefore, in the simulation, the initial temperature was not set to ambient but accounted for this accumulated thermal effect to better reflect the actual conditions observed in the experiment. The translational velocity of the wheel was 16 km/h, and the angular velocity was controlled accordingly to simulate specific slip ratios during braking.

In this study, to address the complexities of the wheel-rail thermal contact phenomenon, both mechanical and thermal solvers were employed in the simulation. During wheel-rail frictional contact (calculated in the mechanical solver), kinetic energy is transformed into heat (calculated in the thermal solver), which consequently induces wheel-rail geometrical changes and affects the temperature-dependent material properties (employed as geometrical and material inputs for the mechanical solver). Concurrent operation and data exchange between the two solvers can be realized via a two-way coupling methodology implemented in LS-DYNA. The computation time steps of the two solvers were as follows: 1.06×10^{-8} for the mechanical solver and 1.00×10^{-6} for the thermal solver. Note that for both solvers, a small computation time step prolongs the computation time, whereas a large time step may induce numerical instabilities.

The governing equation of the mechanical solver involving the thermal effect is defined in Eq. (1) [28,29]:

$$M\ddot{u}(t) + C(T)\dot{u}(t) + K(T)u(t) = F_{ext}(t) + g(T) \tag{1}$$

where t is the time. $\ddot{u}(t), \dot{u}(t)$ and $u(t)$ are the acceleration vector, velocity vector, and displacement vector, respectively. M, $C(T)$, $K(T)$, $F_{ext}(t)$, and $g(T)$ are the mass matrix, damping matrix, stiffness matrix, external mechanical load vector, and thermal load vector, respectively. T is the temperature, which is a function of the time and location of the FE nodes and varies throughout the simulation, as calculated in the thermal solver. Eq. (1) indicates that the damping, stiffness, and thermal load of the model are temperature dependent. This ensures that the thermal effect can be included in the mechanical solver. An explicit time integration scheme [30] was adopted to solve the equation.

The governing equation of the thermal solver is presented in Eq. (2)

Table 3
Temperature-dependent thermomechanical material parameters.

Temperature, T (°C)	Young's modulus, E (GPa)	Poisson's ratio, ν	Coefficient of thermal expansion, α ($\times 10^{-6}$ °C^{-1})	Hardening modulus, Ep (GPa)	Specific heat capacity, c (J/kg°C)	Thermal conductivity, λ (W/m°C)	Yield strength of R260	Yield strength of R350HT
25	209	0.30	11.0	20.9	490.1	6.81	583.0	779.0
100	207	0.30	11.6	20.7	499.9	6.99	583.0	779.0
650	105	0.36	14.8	10.5	571.5	8.26	477.0	673.0
1000	50	0.39	15.7	5.0	617.1	9.06	415.4	611.4
1450	2	0.40	16.1	0.2	671.8	10.91	151.3	347.3

[31,32]:

$$\frac{\partial}{\partial x}\left(k_x\frac{\partial T}{\partial x}\right)+\frac{\partial}{\partial y}\left(k_y\frac{\partial T}{\partial y}\right)+\frac{\partial}{\partial z}\left(k_z\frac{\partial T}{\partial z}\right)+I(x,y,z,t)=\rho c\frac{\partial T}{\partial t} \tag{2}$$

where ρ is the density of the material, and c is the heat capacity. k_x, k_y, and k_z represent the thermal conductivity in the x, y, and z directions, and $I(x,y,z,t)$ represents the internal heat generation rate per unit volume. An implicit method using a generalized trapezoidal time integration algorithm was employed to solve Eq. (2) with given initial and boundary conditions. Because wheel braking was simulated in this study and the wheel-rail interface had been heated due to the braking friction force, an initial temperature of 200 °C was used, i.e., $T^{t=0}_{x,y,z} = 200$ °C. The boundary condition of the thermal contact problem is given in Eq. (3) [31,32] concerning the heat flux boundary (4):

$$k_x\frac{\partial T}{\partial x}n_x+k_y\frac{\partial T}{\partial y}n_y+k_z\frac{\partial T}{\partial z}n_z=Q \tag{3}$$

$$Q=\delta\mu v_s P_{(x,y)} \tag{4}$$

where n_x, n_y, and n_z are the normal vectors in the x, y, and z directions. Q is the heat flux at the nodes due to friction, which relies on the calculations of wheel-rail contact in the mechanical solver. δ is the heat partition to one contact body, and (1- δ) is thus the heat partition to the other contact body. In this model, δ is assumed to be 0.5. μ is the coefficient of friction, and v_s represents the relative sliding velocities of the nodes between the wheel and rail. $P_{(x,y)}$ is the local surface contact pressure. The test was conducted indoors on a laboratory test rig with negligible airflow and a relatively low wheel speed, minimizing convective heat dissipation. Given that radiation and convection occur at a much slower rate compared to thermal conduction, these effects

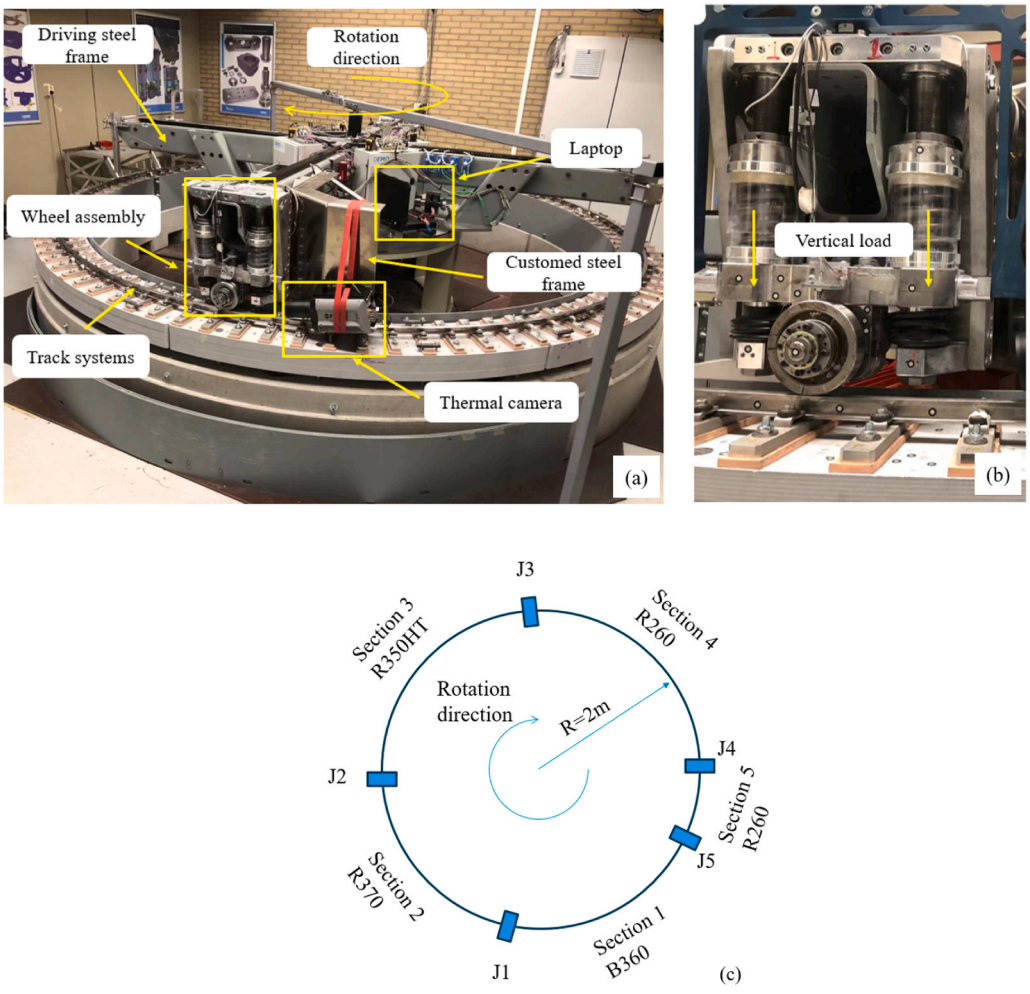

Fig. 2. The V-Track test rig. (a) V-Track components; (b) wheel assembly; (c) schematic drawing of the rail section distribution.

were neglected in the model, as heat primarily conducts into the rail and wheel within the 1.09 ms timeframe, making external heat dissipation mechanisms insignificant.

2.2. Measurement

In this section, the structure of the V-Track test rig is briefly introduced, and the temperature measurement methodology is described. The V-Track test rig is capable of reproducing real-life wheel-rail frictional rolling contact [33] and has been widely employed to investigate related problems [34]. As illustrated in Fig. 2, the V-Track includes a ring track system and two wheel assemblies connected to a driving steel frame that rotates around a vertical axis centred on the ring track. The rails and cylinder wheels used in the V-Track were cut from real-life rail heads and wheel rims, respectively, to ensure identical thermal behaviour. A more detailed description of the V-Track wheel assembly can be found in [26]. The angular velocities of the driving steel frame and the wheel axle were recorded by two separate encoders with a data acquisition rate of 16.67 kHz. Propelled by a motor through the driving steel frame, the wheel assemblies moved at a constant velocity of 16 km/h along the track in this study. The wheel angular velocity was initially controlled to approximately 68.4 rad/s. A braking torque was then applied to one V-Track wheel with another motor to generate the desired slip ratio from 2 % to 35 % and the wheel-rail longitudinal force. At the same time, the temperature field as close as possible to the contact patch was measured. Note that the applications of the braking torque effectively changed the wheel angular velocity but had a trivial influence on wheel assembly translation velocity, which was kept constant by the frame-driving motor. A 4000-N vertical (normal) wheel load, producing a maximum contact pressure of 1.01 GPa, which is similar to that in the field, was applied via the primary suspension of the wheel assembly (shown as two springs in Fig. 2(b)). The angle of attack was designed to be as small as possible to minimize the wheel-rail lateral force. The wheel-rail contact forces were recorded via dynamometers [35] with a data acquisition rate of 16.67 kHz.

As shown in Fig. 2(c), a ring track with a radius R of 2 m is mounted onto 100 uniformly distributed sleepers using fastenings. It consists of five rail sections made of different materials—B360, R370, R350 HT, and R260—that are connected through five rail joints, i.e., J1–J5. The rails have identical profiles, featuring a head curvature radius of 60 mm.

Fig. 3 shows a close-up view of the installation of the thermal camera used to measure the contact temperature in the V-Track. To capture the temperature field as close as possible to the contact patch, a high-speed infrared thermal imaging camera (FLIR X6900sc) was securely mounted on a customized steel frame on the trailing side of the wheel. Moving in synchronization with the wheel assembly, the camera focused on the running band just behind the wheel-rail contact area, enabling the measurement of contact temperature immediately after wheel passage. The thermal camera was connected to a remote-controlled laptop, as shown in Fig. 2(a), for data acquisition. The temperature data were recorded with a sampling frequency of 1 kHz for more than 20 s, during which the wheel assembly ran seven cycles along the track. The measured temperatures, ranging from 250 to 670 °C, were predetermined on the basis of the FE simulation results. The calibrated emissivity value for the rail surface is 0.83 (with a standard deviation of 4 %).

To target the camera as close as possible to the wheel-rail contact area, a small projection angle θ, i.e., the angle between the projection line of the camera and a horizontal line (shown in Fig. 3(b)), is desired. Moreover, to avoid possible collisions between the camera and the rail, a safe distance from the lens to the rail top is needed, which results in an angle of $\theta = 11°$ in this study. The distance from the trailing edge of the camera-targeting patch (denoted by the red solid semicircle in Fig. 3(b)) to the wheel-rail contact patch (denoted by the yellow solid semicircle) can be calculated via Eq. (5):

$$l = r\tan(\arctan(h/d)/2) \tag{5}$$

where l is the distance from the camera-targeting position to the centre of the wheel-rail contact patch, r is the wheel radius, which equals 65 mm, h denotes the distance from the lens centre to the rail top surface, approximately 5.5 mm, and d is the longitudinal distance between the lens centre and the camera-targeting position, which is 28.5 mm. The value of l, which is equal to 6.25 mm, can be calculated via Eq. (5). We use $2a$ to denote the longitudinal length of the contact patch. By dividing (l-a) by the translational wheel speed of 16 km/h, a time lag of the temperature measurement after wheel-rail contact can be obtained, which is 1.09 ms. The simulated contact temperatures after 1.09 ms were thus compared to the measured rail surface temperatures, which will be presented in Section 3.3.

2.3. Slip ratio calculation

The slip ratio is defined as the difference between the translational velocity and the circumferential velocity of the wheel divided by its translational velocity. As mentioned before, two encoders installed in the test rig were applied to record the angular velocity of the driving steel frame ω_d and the wheel axle ω. The translational velocity of the wheel assembly V_p can then be obtained on the basis of the driving steel frame velocity ω_d and ring track radius R according to Eq. (6):

$$V_p = \omega_d \times R \tag{6}$$

However, when Eq. (6) was used to calculate the wheel translation velocity V_p, a sine-wave pattern was observed over the angular position (location as an angle measured from a fixed reference point) along one ring-track circle, as shown by the black curve in Fig. 4. This was a measurement error induced by a slight misalignment between the encoder centre and the rotational centre of the driving steel frame. The

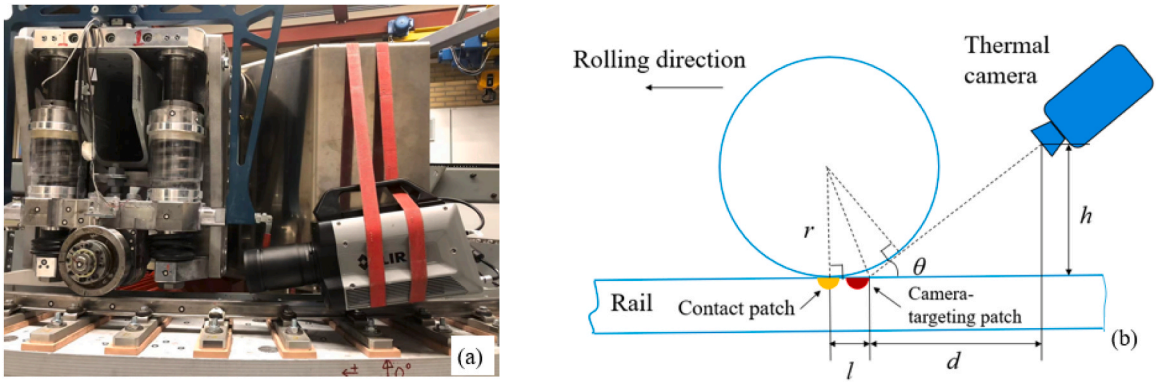

Fig. 3. Installation and position of the thermal camera. (a) Camera installed on a customized steel frame; (b) camera-targeting patch.

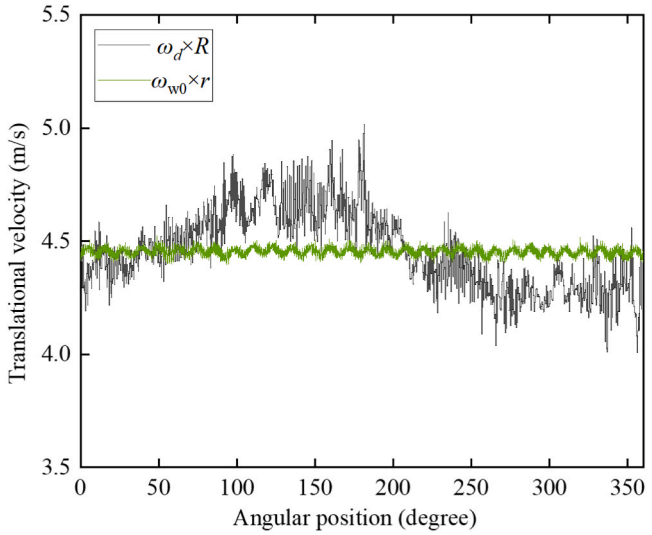

Fig. 4. Two methods to obtain the translational velocity of the wheel assembly during the measurement.

measurement error exceeded 10 %, with an average value of 16 km/h and a maximum value of over 18 km/h, which is unacceptable for the next-step slip ratio estimation, where high-precision velocity measurements are needed.

An alternative method to calculate the wheel translation velocity was thus proposed, as defined in Eq. (7):

$$V_p = \omega_{w0} \times r \tag{7}$$

where ω_{w0} is the angular velocity of the wheel under free rolling contact conditions: a nominal zero longitudinal wheel-rail friction force was achieved by applying a small positive torque to the wheel axle to overcome the negative torque induced by mechanical friction, e.g., from the gearbox. In wheel-rail free rolling contact, the slip ratio is also zero, i.e., the wheel translation velocity equals the wheel circumferential velocity, because the wheel-rail friction force is zero. The measured translation velocity obtained with this alternative method is also presented in Fig. 4, which presents a steady trend along the track circle. Consequently, the measured slip ratio can be calculated via Eq. (8):

$$S = \frac{V_p - \omega r}{V_p} = \frac{\omega_{w0} - \omega}{\omega_{w0}} \times 100\% \tag{8}$$

where S denotes the slip ratio, V_p is the wheel translation velocity, and ω is the wheel angular velocity.

3. Results

3.1. Measurement data processing

A regression analysis was conducted in this study to correlate the measured slip ratio and the temperature during braking. However, because the wheel velocities (and thus the slip ratio calculated on the basis of wheel velocities via Eq. (8)) and temperature data were measured separately, each using separate timing systems, data synchronization was required to conduct the regression analysis accurately. Fig. 5 presents the measured temperature data and the synchronized slip ratio during a wheel braking process. The synchronization method is described below. In Fig. 5, the temperature data points at each instance represent the measured peak temperature within the camera-targeting patch, as presented in Fig. 3(b). The labels S1–S5 and J1–J5 correspond to the rail sections and joints depicted in Fig. 2(b). The moments at which the wheel passes the joints are denoted by the vertical pink dashed lines and were determined from the angular positions along the

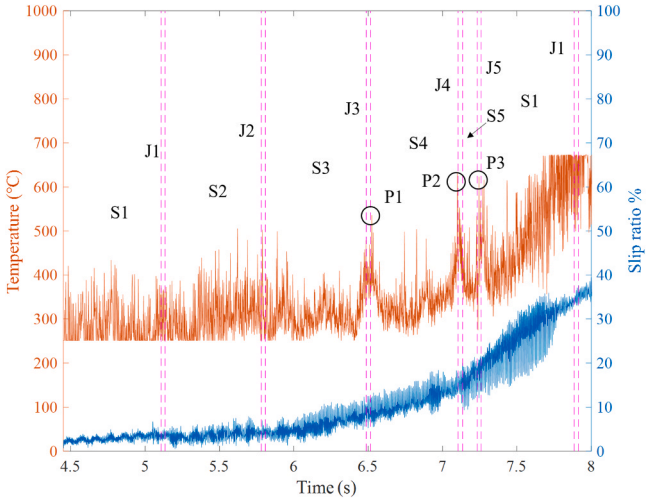

Fig. 5. Maximum temperature within the camera-targeting patch and the slip ratio.

track that were recorded together with the wheel velocities. As illustrated in Fig. 5, the wheel travelled in a braking manner from the rail Section 1 (S1) to Section 4 (S4) between 4.45 s and 7.2 s. Subsequently, after passing Joint 5 (J5) at 7.25 s, the wheel returned to S1 for the next cycle. Throughout the wheel braking process from 4.45 s to 8 s, the temperature increased from 250 °C to 670 °C. Note that the temperature data beyond the predefined measurement range, i.e., from 250 °C to 670 °C, were truncated in the measurement. In the subsequent regression analysis, this truncated data was excluded to ensure accuracy. Correspondingly, the slip ratio, which was calculated via Eq. (8), increased from approximately 2–35 %.

The maximum temperature within the camera-targeting patch and the slip ratio were initially synchronized by shifting the data so that they corresponded at the joints and then assessed with a frequency domain analysis for fine-tuning. The locations of the joints (pink lines) were known for the slip ratio measurement (blue curve) because it was measured together with the wheel angular position along the ring-track circle. The locations of each joint are indicated with two pink vertical lines, one for entry and the other for exit of the joint. In the temperature measurement (orange curve), peaks (P1, P2, and P3 in Fig. 5) were identified at joints of poor quality because such joints have a locally reduced wheel-rail contact area and thus increased contact pressure, increasing the temperature. These joints were J3, J4 and J5. The temperature curve was shifted so that J3, J4 and J5 matched their locations in the slip ratio curve, and the two curves were roughly synchronized.

To obtain more accurate synchronization, a frequency-domain analysis was performed. A power spectral density (PSD) analysis of the measured temperature and slip ratio at S3 is shown in Fig. 6. Both the PSDs of the slip ratio and temperature data exhibit a dominant frequency at 118.5 Hz, denoted by the vertical black dashed line in Fig. 6. This frequency corresponds to the P2 resonance of the wheel-rail system in the V-Track [36] and indicates a notable correlation between the measured temperature data and the slip ratio data. The temperature and slip ratio data were then filtered with passband frequencies of 118–119 Hz. The filtered results before synchronization are displayed in Fig. 7(a).

A correlation analysis was then used to synchronize the measured slip ratio and the temperature by calculating their correlation coefficients P [37] across various time shifts to find the best alignment. P quantifies the linear relationship between two variables, ranging from −1 (fully negative) to + 1 (fully positive). Before the frequency-domain synchronization, P was −0.13, i.e., the case in Fig. 7(a). The measured slip ratio was then incrementally shifted, and the correlation was calculated at each step until P achieved 0.98, as shown in Fig. 7(b),

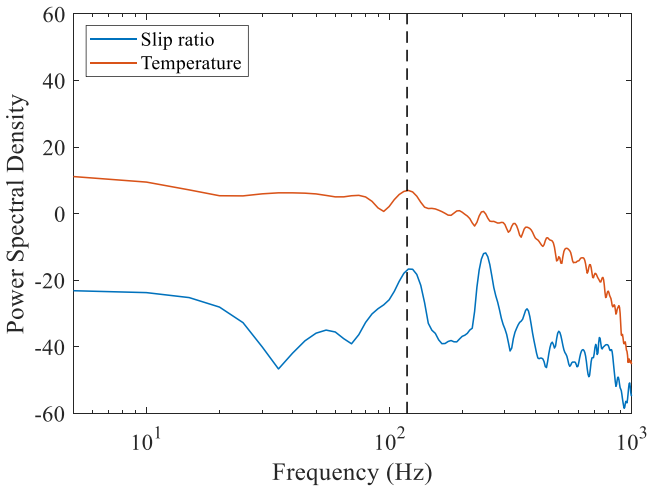

Fig. 6. PSD analysis of the measured slip ratio and temperature of S3.

indicating that the two signals were well synchronized.

3.2. Regression analysis

The analytical model presented in [11] indicates a linear correlation between the slip ratio and the maximum contact temperature when the contact pressure and thermal parameters are constant. Although the temperature measured in this study was not the maximum temperature within the contact patch, but the temperature field immediately behind the contact patch, given the absence of a known relationship, a linear regression analysis was employed to process the measurement data. Future research can be conducted to further characterize this relationship. Based on the linear regression analysis, the correspondence between the measured slip ratio and temperature was obtained via Eq. (9):

$$T = 8.36 \times S + 260 \tag{9}$$

where S and T are the measured slip ratio and temperature (°C), respectively. The coefficient of determination, R^2, was calculated to be 0.72, indicating that approximately 72 % of the variability in the dependent variable T can be explained by the independent variable S in the regression Eq. (9). The temperature T measured from 5.8 s to 7.7 s (mostly ranging between 250 °C and 670 °C) as a function of the slip ratio S, as well as the derived linear regression fitting, are plotted in Fig. 8. The regression equation performs well in fitting the data; therefore, the wheel-rail contact temperatures can be estimated on the basis of this regression equation with input slip ratios. The remaining 28 % of the variability that cannot be explained by the linear regression relationship may be due to the contact pressure varying over time in real-life wheel-rail rolling [38], and the thermal parameters could need to be further calibrated.

3.3. Model validation

3.3.1. Simulation cases and results

The previous section demonstrated the linear correlation between the wheel-rail contact temperature and slip ratio and the possibility of predicting the contact temperature on the basis of the slip ratio. Three slip ratio scenarios—5 %, 10 %, and 15 %—were then simulated via the FE method presented in Section 2.1. In the measurement, we measured the wheel-rail contact temperatures under continuous variation of the slip ratio from low to high along the track with four different rail grades used in the V-Track test rig, as shown in Fig. 2(c). The 5 % and 10 % slip ratio scenarios took place with the rail grade R350HT, and the 15 % slip ratio scenarios occurred with the rail grade R260. To ensure consistency with the experimental conditions, two distinct sets of temperature-dependent material parameters widely used in wheel-rail thermo-mechanical behavior modelling were incorporated into the material modelling. The two material parameter sets, with one set detailed in Tables 1 and 2 and the other in Table 3, result in a total of six simulation cases, as summarized in Table 4. The material parameters provided in Table 1 and Table 3 also illustrate that the same rail type may have different mechanical material parameters at different temperatures, especially the yield strength. The simulated contact temperature on the

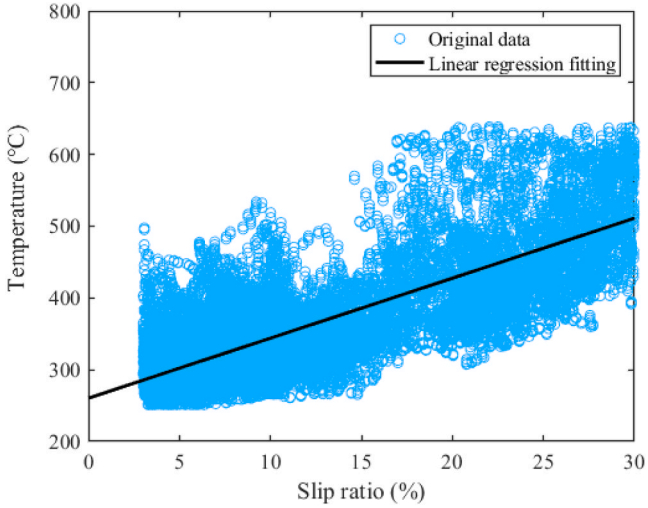

Fig. 8. Linear regression analysis of the measured slip ratio and temperature.

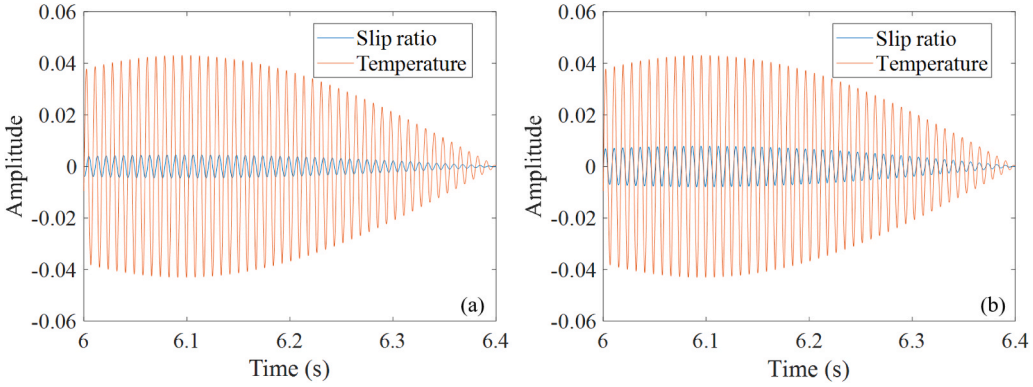

Fig. 7. The bandpass (118 Hz to 119 Hz)-filtered data of the measured temperature and slip ratio. (a) Before frequency-domain synchronization; (b) after frequency-domain synchronization.

Table 4
The simulation cases of the FE model.

Material type	Slip ratio and Rail grade		
Material set of rail (parameters in Table 1&2)	5 %, R350HT (case 1)	10 %, R350HT (case 2)	15 %, R260 (case 3)
Material set of rail (parameters in Table 3)	5 %, R350HT (case 4)	10 %, R350HT (case 5)	15 %, R260 (case 6)

rail along the rolling direction for case 5 (slip ratio =10 % and rail grade R350HT) at 2.7 ms is plotted against the simulated wheel-rail contact pressure in Fig. 9(a).

As shown in Fig. 9(a), the maximum wheel-rail contact pressure during the simulation is 1048 MPa. The peak temperature is 330 °C and occurs at the trailing edge B of the contact patch, whereas the minimum temperature is found at the leading edge A, which is consistent with the findings reported in [11,39]. A gradual increase in contact temperature is observed from the leading area to the trailing area. This is because the wheel and rail materials, with their 'initial temperatures' accumulated in the previous contact cycles, flow into the contact patch from the leading edge, and the contact-induced heat is accumulated during wheel-rail friction rolling until the materials exit the contact patch at the trailing edge.

The temperature-time history of the trailing-edge node in the middle of the contact patch is presented in Fig. 9(b). As mentioned in Section 2.2, the infrared camera employed in this study captured the flash temperatures on the rail head after 1.09 ms of wheel passage; the simulated temperatures were thus extracted 1.09 ms after wheel passage, i.e., 1.09 ms after the peak temperature occurred at the trailing edge of the wheel-rail contact patch, as indicated in Fig. 9(b).

Fig. 10 shows the time histories of the temperature and slip ratio simulated with case 5 (slip ratio = 10 % and rail grade R350HT). As shown in Fig. 10, the simulated slip ratio, calculated via the method presented in [40], fluctuates between 9 % and 11 %, with an average value of 10 %, aligning with the initial setting of simulation case 5. In addition, the simulated temperature also varies with time, with an average temperature of 317 °C and a fluctuation margin of 4 %. This average temperature was then taken as the simulation result to compare with the measured temperature under the same slip ratio conditions. The fluctuations in the simulated slip ratio and temperature should be attributed to the dynamic interactions between the wheel and rail, during which the contact stress and wheel motion vary with time [38].

3.3.2. *Comparison with measurements*

Fig. 11 presents a comparison between the simulated temperatures and the measured temperatures with three different slip ratios and two sets of material parameters. The measured temperatures at different slip ratios were obtained via Eq. (9). The simulation results for all six cases

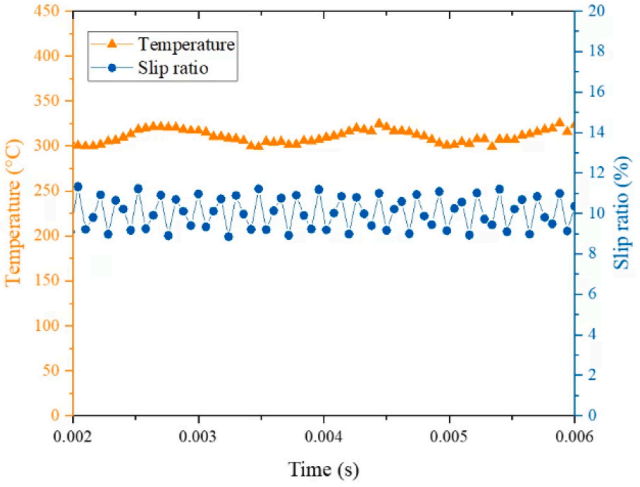

Fig. 10. The time histories of the simulated contact temperature and slip ratio.

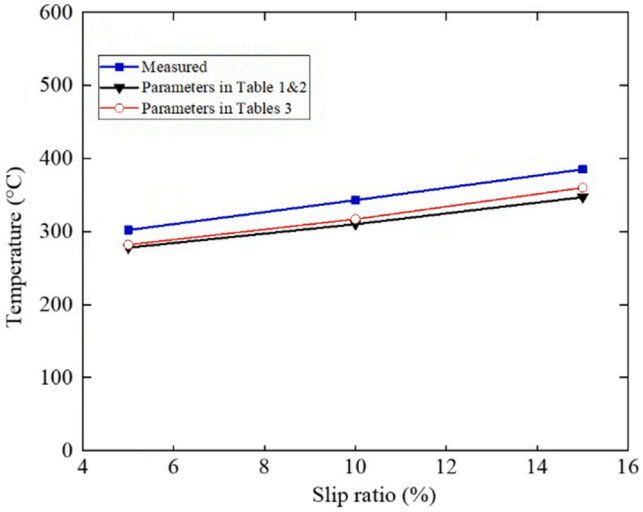

Fig. 11. Comparison of the measured and simulated temperatures with different slip ratios.

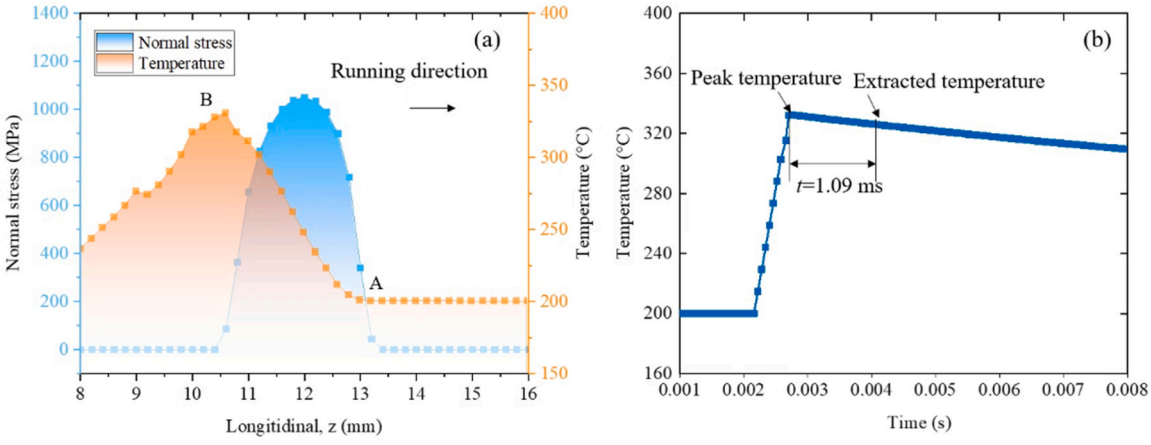

Fig. 9. Numerical solution within the contact patch of case 5 at 2.7 ms. (a) Temperature field and contact pressure on the rail surface; (b) the temperature change over time of the node corresponding to the peak temperature within the contact patch.

were obtained as described in Section 3.3.1.

As shown in Fig. 11, the measured and simulated temperatures exhibit the same increasing pattern as the slip ratio increases from 5 % to 10 % and then to 15 %. The measured contact temperatures are 302 °C, 343 °C, and 385 °C for slip ratios of 5 %, 10 %, and 15 %, respectively. When the material sets from Tables 1 and 2 are used, the simulated temperatures for slip ratios of 5 %, 10 %, and 15 % are 278 °C, 310 °C, and 347 °C, respectively, which are slightly lower than those simulated using the material set from Table 3: 282 °C, 317 °C, and 360 °C. Since the simulated results obtained with the two parameter sets are close to each other and in reasonable agreement with the measurement results, a conclusion can be drawn that both parameter sets can represent the thermomechanical material properties of rail steels when the temperature is below 360 °C.

The maximum relative errors for the cases with the three slip ratios are 7.9 %, 9.6 %, and 9.9 %. The discrepancy increases with the slip ratio and may be because the initial temperature (200 °C) assumed in the simulations for all three slip ratio cases is lower than that under actual conditions. In particular, for the higher slip ratio case (15 %), a higher residual temperature, and thus initial temperature, can accumulate from previous wheel-rail contact cycles. Future work should measure the flash temperature of wheel and rail surfaces immediately before they come into contact, e.g., using an infrared camera targeting the front side of the wheel-rail interface and then providing a more accurate input of initial temperature to the simulation.

4. Conclusions, discussion, and future work

In this study, a thermomechanical finite element (FE) model for simulating wheel and rail interactions during braking was developed with two different temperature-dependent mechanical and thermal material parameter sets. This model was experimentally validated up to approximately 360 °C for the first time on the TU-Delft V-Track test rig under the same contact conditions in terms of the contact pressure, slip ratio and coefficient of friction. After processing the measurement data, including the calculation of the slip ratio and data synchronization, a regression analysis was conducted between the measured contact temperature and slip ratio. Comparisons were then made between the measured and simulated contact temperatures under three high slip ratio scenarios. The following conclusions and insights from the discussion are derived from this study:

1) The contact temperatures simulated with the developed thermomechanical FE model achieve reasonable agreement with the experimental results across slip ratios of 5 %, 10 % and 15 % in terms of the values and variation trends. The maximum error between the simulations and measurements is within 9.9 % up to 360 °C, which is acceptable for engineering applications.
2) The match of the simulated and measured contact temperatures suggests that the proposed model is accurate for simulating wheel-rail contact with thermal effects and that the employed temperature-dependent parameters are reliable for representing the thermomechanical properties of rail materials.
3) A linear relationship was identified between the measured slip ratio and contact temperature. 72 % of the variability in the measured temperature can be explained by the slip ratio in the linear regression equation. The remaining 28 % of the variability that cannot be explained linearly may be due to the contact pressure varying over time during real-life wheel-rail rolling.

The maximum contact temperature is of the most concern in the previous research as it significantly influences contact behavior and the subsequent interface deterioration. In this study, for the experimental validation of the FE thermomechanical model with high slip ratios, which has rarely been addressed in previous research, the contact temperature was measured at a 1.09 ms lag behind the contact patch. The validated FE model then enables the computation of temperature distributions across the contact patch, including the maximum contact temperature. These findings support the reliability of the proposed modelling approach and provide a basis for further investigations into the thermal effects of wheel-rail interactions under high slip conditions.

To further improve the accuracy of the thermomechanical model, more accurate input of the initial temperature of the contact bodies is desirable. In addition, it can be helpful to consider the thermal radiation and convection to the air and the temperature-dependent coefficients of friction. Finally, the thermomechanical model should be better able to account for the contact profile alterations during wheel contact since severe wear can be induced by high slip ratios and elevated temperatures.

CRediT authorship contribution statement

Chunyan He: Writing – original draft, Methodology, Investigation, Formal analysis, Conceptualization. **Zhen Yang:** Writing – review & editing, Supervision, Formal analysis, Conceptualization. **Pan Zhang:** Writing – review & editing, Formal analysis. **Rolf Dollevoet:** Resources, Funding acquisition. **Zili Li:** Writing – review & editing, Supervision, Resources, Funding acquisition, Conceptualization.

Declaration of Competing Interest

The authors declare the following financial interests/personal relationships which may be considered as potential competing interests: Chunyan He reports financial support was provided by Prorail. Chunyan He reports financial support was provided by the China Scholarship Council. If there are other authors, they declare that they have no known competing financial interests or personal relationships that could have appeared to influence the work reported in this paper.

Acknowledgments

The authors thank Jan Moraal, Gokul Jayasree Krishnan and Fang Ren for their assistance in performing the V-Track tests and acquiring the data. This research was partly supported by ProRail and Europe's Rail Flagship Project R2DATO - Rail to Digital automated up to autonomous train operation. Funded by the European Union. Views and opinion expressed are however those of the authors(s) only and do not necessarily reflect those of the European Union. Neither the European Union nor the granting authority can be held responsible for them. This project has received funding from the European Union's Horizon Europe research and innovation programme under Grant Agreement No 101102001. This work was partly supported by the China Scholarship Council.

Data availability

Data will be made available on request.

References

[1] Ekberg A, Kabo E. Fatigue of railway wheels and rails under rolling contact and thermal loading—an overview. Wear 2005;258:1288–300. https://doi.org/10.1016/j.wear.2004.03.039.
[2] Srivastava JP, Sarkar PK, Ranjan V. Effects of thermal load on wheel–rail contacts: a review. J Therm Stress 2016;39:1389–418. https://doi.org/10.1080/01495739.2016.1216060.
[3] Asih AMS, Ding K, Kapoor A. Modelling rail wear transition and mechanism due to frictional heating. Wear 2012;284-285:82–90. https://doi.org/10.1016/j.wear.2012.02.017.
[4] Ahlström J, Karlsson BJW. Analytical 1D model for analysis of the thermally affected zone formed during railway wheel skid. Wear 1999;232:15–24. https://doi.org/10.1016/S0043-1648(99)00167-2.
[5] Ertz M, Knothe K. Thermal stresses and shakedown in wheel/rail contact. Arch Appl Mech (Ing Arch) 2003;72:715–29. https://doi.org/10.1007/s00419-002-0255-4.

[6] Bernsteiner C, Müller G, Meierhofer A, Six K, Künstner D, Dietmaier P. Development of white etching layers on rails: simulations and experiments. Wear 2016;366-367:116–22. https://doi.org/10.1016/j.wear.2016.03.028.
[7] Jergéus J, Odenmarck C, Lunden R, Sotkovszki P, Karlsson B, Gullers P. Full-scale railway wheel flat experiments. Proc Inst Mech Eng, Part F: J Rail Rapid Transit 1999;213:1–13. https://doi.org/10.1243/0954409991530985.
[8] Lian Q, Deng G, Tieu AK, Li H, Liu Z, Wang X, Zhu H. Thermo-mechanical coupled finite element analysis of rolling contact fatigue and wear properties of a rail steel under different slip ratios. Tribology Int 2020;141:105943. https://doi.org/10.1016/j.triboint.2019.105943.
[9] Jaeger J. Moving sources of heat and temperature at sliding contacts. Proc R Soc N South Wales 1942;76:222.
[10] Blok H. The flash temperature concept. Wear 1963;6:483–94. https://doi.org/10.1016/0043-1648(63)90283-7.
[11] Knothe K, Liebelt SJW. Determination of temperatures for sliding contact with applications for wheel-rail systems. Wear 1995;189:91–9. https://doi.org/10.1016/0043-1648(95)06666-7.
[12] Lewisa R, Dwyer-Joyce R. Wear mechanisms and transitions in railway wheel steels. Proc Inst Mech Eng, Part J: J Eng Tribology 2004;218:467–78. https://doi.org/10.1243/1350650042794815.
[13] Olver A. Testing transmission lubricants: the importance of thermal response. Proc Inst Mech Eng Part G: J Aerosp Eng 1991;205:35–44. https://doi.org/10.1243/PIME_PROC_1991_205_235_0.
[14] Naeimi M, Li S, Li Z, Wu J, Petrov RH, Sietsma J, Dollevoet R. Thermomechanical analysis of the wheel-rail contact using a coupled modelling procedure. Tribology Int 2018;117:250–60. https://doi.org/10.1016/j.triboint.2017.09.010.
[15] Vo K, Tieu AK, Zhu H, Kosasih P. The influence of high temperature due to high adhesion condition on rail damage. Wear 2015;330:571–80. https://doi.org/10.1016/j.wear.2015.01.059.
[16] Goldak J, Chakravarti A, Bibby M. A new finite element model for welding heat sources. Metall Trans B 1984;15:299–305. https://doi.org/10.1007/BF02667333.
[17] Gallardo-Hernandez EA, Lewis R, Dwyer-Joyce RS. Temperature in a twin-disc wheel/rail contact simulation. Tribology Int 2006;39:1653–63. https://doi.org/10.1016/j.triboint.2006.01.028.
[18] Petereson M. Two-dimensional finite element simulation of the thermal problem at railway block braking. Proc Inst Mech Eng, Part C: J Mech Eng Sci 2002;216:259–73. https://doi.org/10.1243/0954406021524945.
[19] Vernersson T. Temperatures at railway tread braking. Part 1: modelling. Proc Inst Mech Eng, Part F: J Rail 2007;221:167–82. https://doi.org/10.1243/0954409JRRT57.
[20] Vernersson T, Lundén R. R. Transit, Temperatures at railway tread braking. Part 3: wheel and block temperatures and the influence of rail chill. Proc Inst Mech Eng, Part F: J Rail 2007;221:443–54. https://doi.org/10.1243/09544097JRRT91.
[21] Baranowski P, Damaziak K, Malachowski J, Mazurkiewicz L, Polakowski H, Piatkowski T, Kastek M. Thermovision in the validation process of numerical simulation of braking. Metrol Meas Syst 2014;21:329–40. https://doi.org/10.2478/mms-2014-0028.
[22] Chen YC, Lee SY. Elastic-plastic wheel-rail thermal contact on corrugated rails during wheel braking. J Tribology 2009;131(1):011401. https://doi.org/10.1115/1.2991163.
[23] Wu L, Wen Z, Li W, Jin X. Thermo-elastic–plastic finite element analysis of wheel/rail sliding contact. Wear 2011;271:437–43. https://doi.org/10.1016/j.wear.2010.10.034.
[24] Wei Y, Wu Y, Chen Z. An experimental measurement and numerical calculation method on friction temperature rise of sliding contact pairs - taking rail/wheel contact as an example. J Meas Eng 2023;11:1–11. https://doi.org/10.21595/jme.2023.22974.
[25] Talamini B, Gordon J, Perlman AB. Investigation of the effects of sliding on wheel tread damage. ASME Int Mech Eng Congr Expo 2005;42210:119–25.
[26] Naeimi M, Li Z, Petrov RH, Sietsma J, Dollevoet R. Development of a new downscale setup for wheel-rail contact experiments under impact loading conditions. Exp Tech 2017;42:1–17. https://doi.org/10.1007/s40799-017-0216-z.
[27] Zhao X, Li Z. The solution of frictional wheel–rail rolling contact with a 3D transient finite element model: validation and error analysis. Wear 2011;271:444–52. https://doi.org/10.1016/j.wear.2010.10.007.
[28] Jain S, Tiso P. Model order reduction for temperature-dependent nonlinear mechanical systems: a multiple scales approach. J Sound Vib 2020;465. https://doi.org/10.1016/j.jsv.2019.115022.
[29] Hsu TR. The finite element method in thermomechanics. Springer Science & Business Media; 2012.
[30] Yang Z, Deng X, Li Z. Numerical modeling of dynamic frictional rolling contact with an explicit finite element method. Tribology Int 2019;129:214–31. https://doi.org/10.1016/j.triboint.2018.08.028.
[31] John OH. LS-DYNA theory manual. California: Livermore Software Technology Corporation; 2006.
[32] Özışık MN. Heat Conduction. Wiley; 1980.
[33] Yang Z, Zhang P, Moraal J, Li Z. An experimental study on the effects of friction modifiers on wheel–rail dynamic interactions with various angles of attack. Railw Eng Sci 2022;30:360–82. https://doi.org/10.1007/s40534-022-00285-y.
[34] Zhang P, Li Z. New experimental evidences of corrugation formation due to rail longitudinal vibration mode. Int J Rail Transp 2024:1–22. https://doi.org/10.1080/23248378.2024.2336503.
[35] Zhang P, Moraal J, Li ZJM. Design, calibration and validation of a wheel-rail contact force measurement system in V-Track. Measurement 2021;175:109105. https://doi.org/10.1016/j.measurement.2021.109105.
[36] Zhang P, He C, Shen C, Dollevoet R, Li Z. Comprehensive validation of three-dimensional finite element modelling of wheel-rail high-frequency interaction via the V-Track test rig. Veh Syst Dyn 2024:1–25. https://doi.org/10.1080/00423114.2024.2304626.
[37] Pearson K. X. On the criterion that a given system of deviations from the probable in the case of a correlated system of variables is such that it can be reasonably supposed to have arisen from random sampling. Lond, Edinb, Dublin Philos Mag J Sci 2009;50:157–75. https://doi.org/10.1080/14786440009463897.
[38] Yang Z, Li Z. Numerical modeling of wheel-rail squeal-exciting contact. Int J Mech Sci 2019;153-154:490–9. https://doi.org/10.1016/j.ijmecsci.2019.02.012.
[39] Alizadeh Otorabad H, Younesian D, Hosseini Tehrani P, Sietsma J, Petrov R. Modeling temperature evolution of wheel flat during formation. Int J Therm Sci 2019;140:114–26. https://doi.org/10.1016/j.ijthermalsci.2019.02.040.
[40] Zhao X, Wen Z, Zhu M, Jin X. A study on high-speed rolling contact between a wheel and a contaminated rail. Veh Syst Dyn 2014;52:1270–87. https://doi.org/10.1080/00423114.2014.934845.